THESIS

ATOMIC FORCE MICROSCOPY: MORE THAN SURFACE IMAGING

Submitted by

Terrance Tyler Bishop

Department of Biomedical Engineering

In partial fulfillment of the requirements

For the Degree of Master of Science

Colorado State University

Fort Collins, Colorado

Summer 2020

Master's Committee:

Advisor: Diego Krapf

Ashok Prasad
Alan Van Orden

ABSTRACT

ATOMIC FORCE MICROSCOPY: MORE THAN SURFACE IMAGING

Atomic Force Microscopy (AFM) is a powerful imaging tool that has capabilities that go beyond the abilities of most other microscopes. Here, three examples of these capabilities were considered. First, the AFM was operated in an image generating mode to determine the surface heterogeneity of polysaccharide membranes. Second, the AFM was used to record force-indentation curves, these curves were fit with a Hertzian model to determine the stiffness of murine smooth muscle cells. Finally a approach for attaching 10 μm and 2 μm polystyrene beads to tip-less AFM cantilevers was proposed, and a viscoelastic contact model was tested to determine the viability of the created probes.

ACKNOWLEDGEMENTS

I would like to thank my advisor Dr. Krapf for taking a chance on me and giving me the opportunity to learn and grow with his lab. Thank you to Ellen, Jacqui, Sara, and Brett for their endless support and understanding. Additionally I would like to thank all of the people I collaborated with to make this thesis a reality. From the HeLa cell source our lab used, to Adam Greenburg helps 3d printing, to the visiting scientists that wanted some AFM data. This thesis wouldn't have been possible without the power of collaboration. Finally, thank you to my thesis committee for your patience.

DEDICATION

I would like to dedicate this thesis to my parents, my partner Dev, and my cats Cappuchino and Huxley. The Marathon Continues.

TABLE OF CONTENTS

LIST OF TABLES

LIST OF FIGURES

Chapter 1

Overview of AFM Tools

1.1 Motivation

Since its invention in the late 1980's the Atomic Force Microscope (AFM) has become a staple of nanotechnology. Where investigation of nanoscale material typically was burdensome, the AFM has provided an avenue for these measurements to be conducted in a repeatable manner. AFM's operating principle relies on the ability of a cantilever with a sharp tip to register small interatomic forces. Conversely, the cantilever needs to be unresponsive to outside disturbances from the environment, like building vibrations. AFM has demonstrated to be advantageous for a number of reasons, likely the most powerful of which is the nature of the interaction between the sample and the tip. Because the tip physically interacts with the sample the tip can be functionalized depending on application. A few examples of applications are given below

- A sharp tip can generate topology images with angstrom precision
- Force spectroscopy, proteins can be pulled on to determine their folding energy [1]
- A tip can be magnetized to determine the strength of a magnetic interaction [2]
- A fast scanning AFM can visualize cell dynamics like migration or mitosis [3]

The difference between these applications depends on the operation mode of the AFM and the functionalization of the tip. The AFM's micro fabricated cantilever with a tip is highly customizable allowing for innovative and dynamic research. The AFM typically includes the following components: a cantilever with a tip, a stage for placing samples on, a laser and a photodiode detector. See Figure 1.1

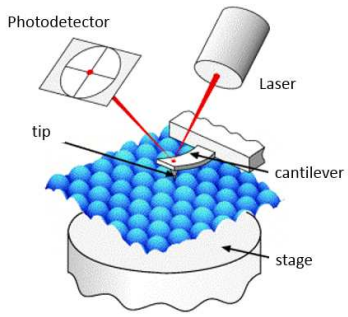

Figure 1.1: Schematic of a Atomic Force Microscope. The tip pyshically interacts with the sample, this interaction is measured by a photodectector which records the laser signal reflected from the top of the cantilever. The stage can be used to move the sample or the cantilever depending on the AFM. [5]

1.2 AFM Background

In a typical AFM system a laser beam is reflected from its point of origin off the cantilever and towards a four quadrant photodetector. A four quadrant detector allows for detection of interatomic forces in both the lateral and vertical directions. As the AFM interacts with the sample the position and intensity of the reflected beam is recorded on the detector. [4] The information recorded by this detector can be used differently depending on the operation mode of the AFM.

The next section will take the ideas introduced above and discuss the main operation modes for the AFM. Whether the goal is to visualize cell dynamics, or generate topology images the mode of operation becomes exceedingly important.

1.3 Operation Modes

The AFM is operated in three main modes: Contact, Non-contact and Tapping. Each mode allows for the behavior of the tip to be controlled depending on the desired application. The primary difference between these operation modes is the way the AFM interprets the different feedback signals available to it. For example, the AFM can measure the total signal change as the cantilever reflects its laser or it can measure the phase of the oscillation amplitude of the cantilever as it changes. Both of these different ways of interpreting information lead to strengths and weakness

Table 1.1: Table of the three most common AFM operation modes, adapted from [6]

Mode	Feedback	Principle	Advantages
Contact	Cantilever Signal	Cantilever signal is adjusted to keep tip in close contact with the sample.	High-resolution images.
Intermittent Contact (Tapping mode)	Oscillation Amplitude	The probe is oscillated in such a way the tip makes repulsive contact with the sample at the lowest point of the oscillation.	Phase of the cantilever oscillation can give additional information about the sample.
Non-Contact	Oscillation Amplitude	Probe oscillated at a distance away from the sample, attractive interaction between the sample and the tip	Minimal damage to the sample

for each functionality. An example of the three main modes and the differences between each are given in Table 1.1

In the work presented here, contact and tapping mode were used. Tapping mode was used to generate topographic images, while contact mode was used for the force-indentation experiments. Topographic images are generated by recording the height of the sample relative to the probe and factoring in the known tip-sample interaction. The simplest tip-sample interaction force can be modeled as a Lennard-Jones force [7]

$$\mathbf{F}(r) = -\frac{6\mathbf{A}}{r^7} + \frac{12\mathbf{B}}{r^{13}}, \tag{1.1}$$

Where r is the separation between the tip and the sample and A and B are constants. The $\frac{6\mathbf{A}}{r^7}$ term models the Van Der Waals interactions which captures the attractive force between the atoms of the sample and the tip. These forces become perceptible when r<10nm. At separations smaller than 1 Å the atoms in the cantilever and in the sample experience strong repulsive forces due to the overlap of electron clouds. In liquid ionic interactions also come into play. This repulsive force is accounted for by the $\frac{12\mathbf{B}}{r^{13}}$ term.

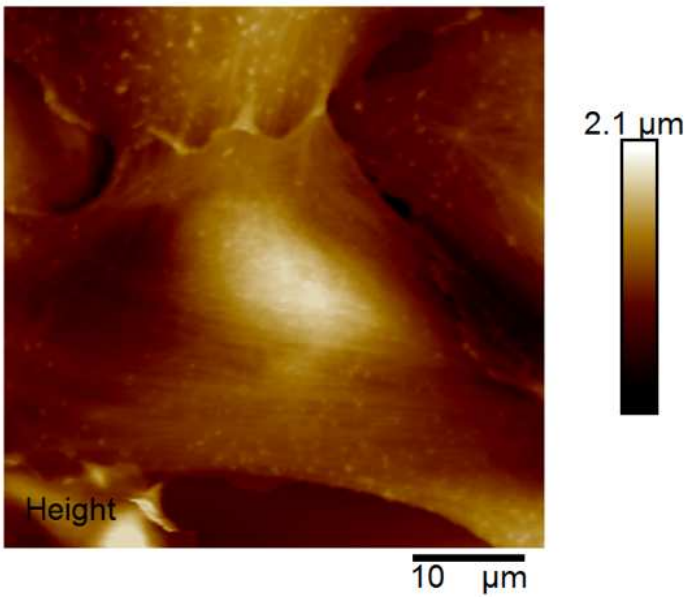

Figure 1.2: Topographic image of a mouse smooth muscle cell. Note the cable like cytoskeletal features. Image taken in tapping mode.

1.4 Surface Topology

The AFM can be used to generate topographic images for both qualitative and quantitative applications. In our lab surface topography images are typically used as a qualitative check, preceding force indentation measurements, as a means of checking to see if the cell is healthy. If the cell looks good the topology scan is used to pick a location for force indentation cycles to be conducted. A example of one such topographic image taken from a mouse smooth muscle cell is included in Figure 1.2.

1.5 Calibration to Obtain Force Data

The AFM is a powerful tool for mechanobiology because it is highly sensitive, allows for precise positioning of the tip with respect to the sample and it can be operated in physiological environments. The physiological environments which are essential to in vivo research can be operated for extended periods in AFM, and also can be modified to allow perfusion of new treatments without exposing the sample to contamination. Experiments conducted in tapping mode, intermittent contact with the sample, are ideal for generating topological images. If AFM is operated

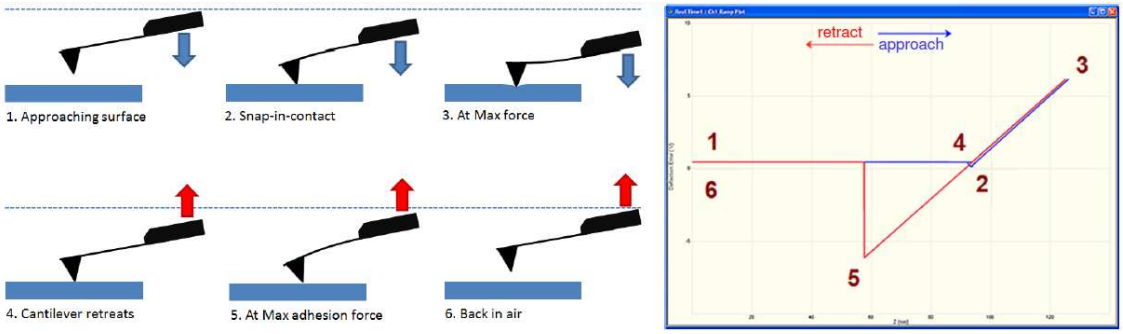

Figure 1.3: Left) Cantilever behavior during the approach-retract cycle. Right) Deflection Error vs Distance. Adapted from [10]

in contact mode the probe can be indented into a sample while recording the force on probe as a function of the probes displacement. These force displacement curves can be fit to a variety of models and different parameters can be extracted depending on which model is fit to the data. In this thesis the focus will be on extracting measures of cell stiffness and cell viscoelasticity.

For a stiff sample the deflection of the cantilever is proportional to the sample height while the tip is in contact with the sample. For soft samples the tip may deform as loading force is in increased, leading to a difference between the movement of the tip and the sample base, this difference is called indentation $=\delta$. This indentation can be reversible, irreversible or viscous (or some combination of all three) in nature [8]. In this thesis we will begin with a model that characterizes how stiff a sample is (Hertzian Model), and secondly a model which is capable of describing the viscoelastic behavior of a sample (the solution for a viscoelastic sample with a rigid spherical indenter [9]).

Force-indentation measurements can be carried out in a variety of manners. Typically the cantilever is driven by the scanner piezo through a sinusoidal extension and retraction cycle. This cycle is carried out below the resonate frequency of the cantilever. A example force curve on a hard sample is given along with the cantilever behavior in Figure 1.3.

Force-indentation curves can be fit with models that utilize the tip-sample interaction in order to extract material properties. However, before that can be done the cantilever must be calibrated for the information obtained to be quantitative. There are three necessary calibrations: deflection sensitivity, the spring constant, and the tip radius. The specifics of each calibration can be found

in appendix B, the focus here is to roughly introduce the calibration and what information it gives us. Deflection sensitivity is calibrated by conducting a force-indentation cycle on a sample that is harder than the sample measurements will be conducted on. This process gives the ratio of known cantilever movement as determined by the Z piezo to the photodetector signal output. The second calibration is called a thermal tune, the cantilever probe is oscillated at a range of frequencies including its resonate frequency in order to determine the cantilever's spring constant. The final calibration is a experimental determination of the radius of the probe tip. Once these calibrations have been performed quantitative measurements can be conducted. The next section will describe the process we conducted for measuring the mechanical properties of soft materials and present selected results

Chapter 2

Measurement of Mechanical Properties of Soft Materials

2.1 Introduction

It has so it has been established that the AFM is a tool for inspecting surface morphology and also that the AFM can be used for probing the physical properties of samples. It has been shown that the material properties of cells can be indicative of disease states such as cancer [11] . The ability to inspect surface morphology and physical properties sets the stage for the AFM to be a useful tool to probe and understand the relationship between material properties and disease states.

One such example is the sarcomeric protein titin and its role in a variety of disease states. Titin is a key determinant of myocardial passive stiffness and stress sensitive signaling. The stiffness of titin is moderated by isoform variation, phosphorylation and potentially through disulfide bond formation [13]. Titin has two major classes of isoforms, N2BA and N2B. N2BA titin is large and compliant, while N2B titin is smaller and stiffer. It has been seen that mutations to titin have lead to a number of different disease states include dilated cardiomyopathy (DCM) and hypertrophic cardiomyopathy [14]. RNA binding motif protein 20 (RBM20) is a gene for hereditary cardiomyopathy which regulates titin splicing. Alternative splicing has been shown to serve a highly useful purpose in cardiac adaptive responses. Specifically, in this case alternative splicing leads to a iso-

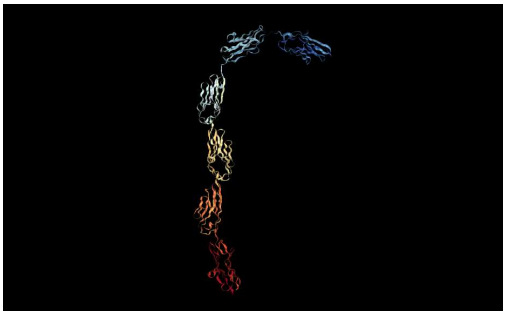

Figure 2.1: 3D representation of titin Adapted from [12]

form switch of titin which leads to adjustments in ventricular filling [15]. Finally it was shown that upregulation of compliant forms of titin resulted in passive stiffness changes in DCM cardiac muscle. [16].

RBM20 is a muscle specific splicing factor that has been implicated in DCM. Loss of function in RBM20 could result in mis-splicing of muscle genes, specifically titin. In the heart, RBM20 mutation induces only larger N2BA titin expression. It is hypothesized that based on the spring equation, the increased length of the titin isoform under otherwise the same physiological conditions will result in decreased myocardial wall stiffness.

Since RBM20 and titin are also expressed in smooth muscle, it would be interesting to know whether RBM20 could regulate aortic smooth muscle stiffness through titin isoform expression as it does in cardiac muscle. Therefore, the purpose of this study is to determine the role of RBM20 in regulating aortic smooth muscle stiffness in the development of hypertension. It is hypothesized that RBM20 knockout induces larger titin isoform expression in aortic smooth muscle and thus reduces aortic smooth muscle stiffness.

2.2 Analysis

To obtain physical data from the probe-sample interaction it is necessary to consider the models that describe the physics at the tip-sample interface. Within the Hertzian model, the indenter is assumed to be a sphere and the surface is assumed to be flat. The Hertzian models relates force (F) to elastic modulus (E) and indentation (δ) given the force is applied with a known radius (R) and Poisson ratio (ν). Poisson ratio is defined as the ratio of transverse to axial strains, $\nu = -\epsilon_{trans}/\epsilon_{axial}$. It is usually between 0.1< ν <0.5. Here elastic modulus (aka Young's modulus) E is the ratio between stress and strain. Young's modulus refers to the slope of a stress vs. strain curve within the elastic region.

$$\mathbf{F}(\delta) = \frac{4}{3}\frac{E}{1-\nu^2}\sqrt{R\delta^3} \tag{2.1}$$

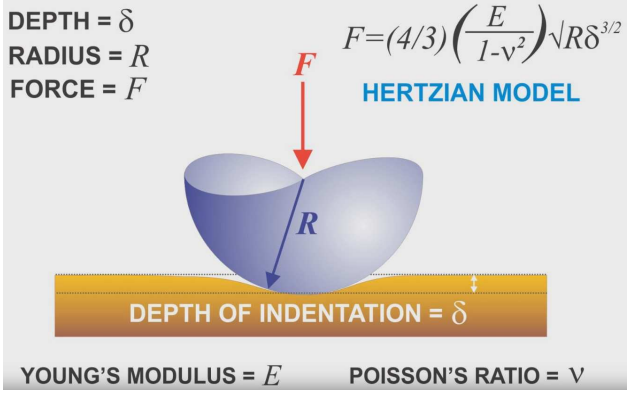

Figure 2.2: Hertzian model for a spherical indenter Adapted from [10]

Here, force is not linear with indentation due to the spherical shape of the indenter. As the indentation depth increases, so does the area of the indenter. In this case, where the elastic modulus is determined from the slope of a stress-strain curve the elastic modulus is a measure of an objects stiffness. Additionally, a material is elastic if the stress-strain curve is identical for loading vs unloading, and if the stress depends only on the current strain not the history [17]. For many materials, particularly biologic materials, the stress-strain curve is non-identical and the stress depends upon the loading history. Fung showed that for rabbit mysentry the Young's modulus is essentially zero at small strain but increases exponentially as with the strain [18]. The stress strain curves of these materials combine a unique stress-strain relationship which is related to the elasticity of the material, but there is also a history dependent aspect which is related to stress relaxation, creep, hysteresis. Materials that show this combination of an elastic response with a time dependence are viscoelastic materials.

A sample force curve is given in Figure 2.3. The blue curve is the raw force curve data and the red line is the Hertzian's model fit. Besides assuming a flat surface and a spherical indenter the Hertzian model has a few assumptions

- The strains are small and within the maximum force per unit area the material can withstand before permanent deformation occurs
- The surfaces are continuous and frictionless

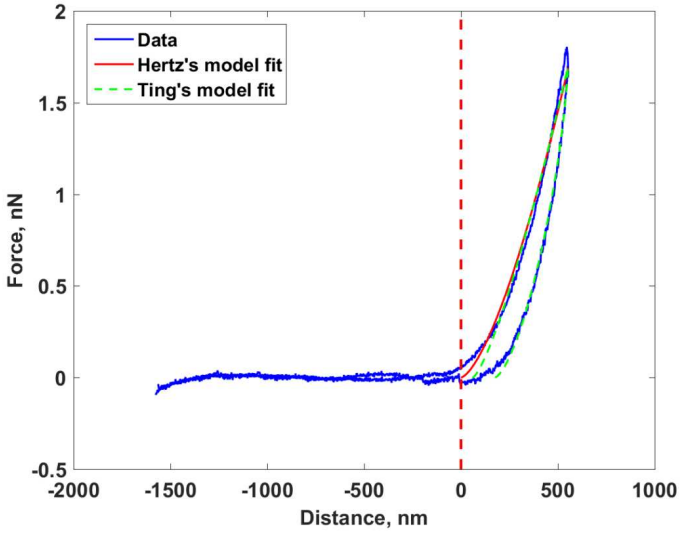

Figure 2.3: Example Force (nN) indentation (nm) curve taken on a HeLa Cell. The blue curve is the raw AFM data. The dashed red line indicates the contact point, or the start of the tip-sample interaction. The solid red line depicts the Hertzian fit to the raw data.

- Each body can be considered as a elastic half space
- The Hertzian model assumes purely elastic sample behavior

The Hertzian model fits the linear region of the indentation curve and can be used to extract the Young's modulus for a material. In some cases another model will be needed to capture the difference in the behavior between the approach and retract region. As mentioned above the Hertzian model assumes purely elastic behavior, meaning between the approach and retract cycles would be identical. Physically, the identical behavior of the approach and retract cycle would translate to no energy lost between loading and unloading. A quick inspection of the Figure 2.3 shows that our material behaves more like a viscoelastic material than one that is purely elastic. From visual inspection the most telling sign that the material is viscoelastic is the difference between the approach and retract curves, known as hysteresis. The evidence of this hysteresis almost immediately suggests that more complicated models than the Hertzian one could be applied to extract additional information from the system.

2.3 Experiments

In this section two experiments are presented along with their results. The first experiment involves using surface topology to determine the surface heterogeneity of polysaccharide membranes. The second experiment involves fitting a Hertzian model to the force-indentation curves taken on murine smooth muscule cells. The first experiment was done in collaboration with Jéssica Martins, Samira Camargo, Ketul Popat, Matt Kipper, and Alessandro Martins. Ketul Popat and Matt Kipper are colloborators within the Colorado State University's school of biomedical engineering, while Jéssica Martins, Alesandro Martins and Samira Camargo are collaborators from post graduate programs from the Federal Unversity of Technology in Apucarana, Brazil. The second set of experiments was done in collaboration with Wei Guo and Chaquon Zhu from the University of Wyoming.

2.3.1 Surface Uniformity of Hydrogels

One of the strengths of atomic force microscopy is the variety of data that can be collected. It can be used to characterize a material's properties and to visualize a material's surface. The ability to obtain these different types of measurements makes the AFM a powerful tool because the properties of a material [19] and the the surface topology [20] have real biologic consequences. For the first experiment, the uniformity of the surface topology was under examination.

Pectin and chitosan have anti-inflamatory, cytocompatibility, and biodegradable properties, and they can be assembled to produce physical hydrogel membranes via acquisitions of poly-electrolyte complexes (PECs) [21, 22]. One advantage of using PEC-based materials is that they can be produced without the toxic crosslinking agents typically necessary to create hydrogels. [23, 24]. The goal of the project was to expand on the characterization of pectin/chitosan (PT/CS) membranes, and to report suitable PT/CS weight ratios for obtaining PEC membranes with high stability, tensile strength, cytocompatability and ability to support human adipose-derived stem cell culture. The hydrogels were created using a method recently proposed by the collaborators. [25] Two ratios of PT/CS were fully characterized, their ratios are include in Figure 2.1 [25]

Table 2.1: Ratio of PT/CS for the two hydrogels that were tested in this study.

Samples	PT (mL:mg)	CS (mL:mg)	Blend	PT/CS ratio	Yield (%)
M(25-5)	25:250	5:50	30	6 ± 3	85 ± 4
M(20-10)	20:200	10:100	2.5	0.8 ± 3	93 ± 2

2.3.2 Modulus Measurements on Smooth Muscle

It was hypothesized by Wei Guo and Chaquon Zhu that a RBM20 knockout would result in reduced aortic smooth muscle stiffness. AFM measurements were conducted initially in tapping mode. First a topographic image of a cell was created to ensure scans were being conducted in a uniform area. Then at least 100 force-indentation cycles were taken for each cell. Measurements were conducted on 45 wild-type cells a d 35 RBM20 knockout cells. The force curves were put through an auto-analysis program using Bruker's NanoScope Analysis. The Auto-program first displays the force curve as Deflection error vs Height sensor output. Then, a baseline correction is applied so that the force curve is normalized by region of the force curve where the cantilever is not interacting with the sample. This region without interaction is set to zero force. Finally a Hertzian model is fit to the approach region of the force curve. Parameters like goodness of fit, tip velocity during the indentation cycle, contact point and most importantly the Young's modulus are provided as output.

2.4 Results

2.4.1 Surface Uniformity-Results

For the purpose of this thesis AFM results will be primarily considered, but the membranes were also characterized by the following means:

- X-ray photoelectron spectroscopy (XPS)- determination of the surface chemistry of the membrane

- Scanning Electron Microscopy (SEM)- used in addition to AFM to investigate surface morphology
- Mechanical Analysis- thickness was measured using a digital micro-durometer and tensile properties were determined using the Stable Microsystems texture analyzer
- Water contact angle measurements
- Cytocompatability assays- First cells were cultured, the cytotoxicity of the PEC membranes were determined, and adhesion and proliferation tests were conducted

AFM was used as a tool to investigate the surface morphology of dry membranes. The measurements were conducted in tapping mode, in Air, using a ScanAsyst probe recording at a rate of one line scan per second.

Figure 2.4 shows the AFM images of the PEC membranes. The topology of the surface displays structural homogeneity at the sub micron length scale, featuring compact traits without cavities and projections, owing to the strong association between PT and CS chains. It was shown that tuning the ratio of PT/CS enhanced mechanical strength, and modulated the hydrophobicity and cytocompatability. The membranes were able to be tuned to have a ultimate tensile strength similar to human skin, a tenfold improvement from previously reported values [26].

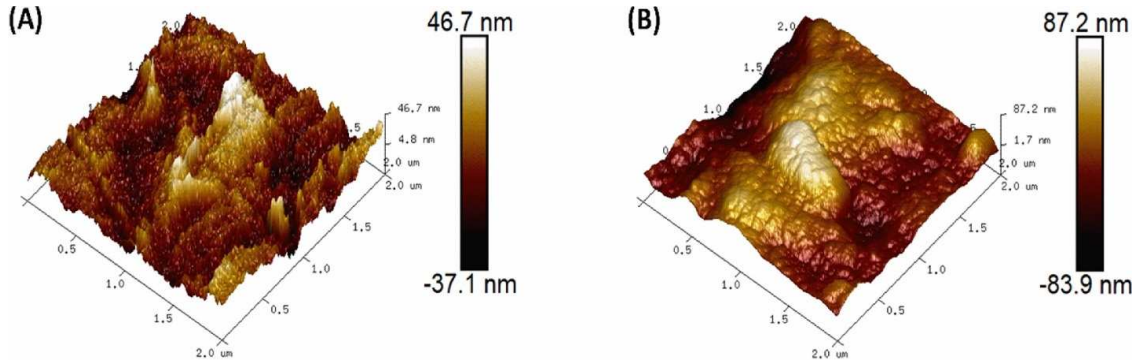

Figure 2.4: AFM topology images for the M(20-10) (A) and M(25-5) (B) membranes

2.4.2 Modulus Measurements on Smooth Muscle-Results

The goal here was to look at the stiffness of the wild type smooth muscle cells compared to the stiffness of the RBM20 knockout. This was done by fitting a Hertzian model to force-indentation curves in order to extract the Young's modulus of the cell. Measurements were taken on 45 wild type cells and 35 knock out cells. For each cell 100 indentation cycles were conducted.

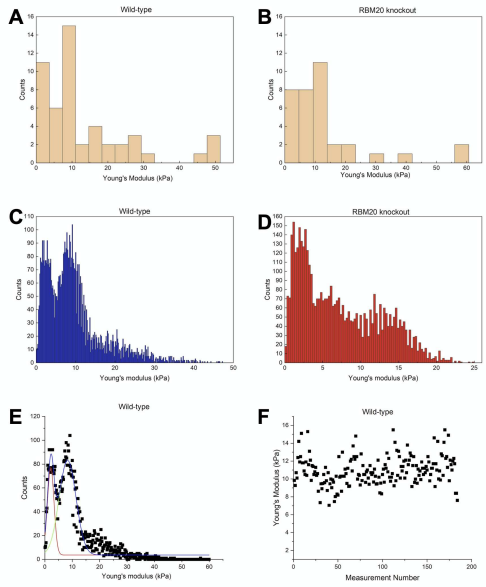

Figure 2.5: A) Histogram for the average modulus for each wild-type cell B) Histogram for the average modulus for each RBM20 knockout cell. C) Histogram of all measurements for wild-type cells D) Histogram of all measurements on RBM20 knockout cells. E) Binomial distribution fit to the histogram of all measurements for wild-type measurements. Information on fit equation in appendix E. F) Measurement history for an individual cell.

The average Young's modulus for the wild-type cells was determined to be $9.51 \pm .09$, while the average Young's modulus for the RBM20 knock out is $7.26 \pm .08$. Anova analysis in Origin confirms that at the 0.05 level the population means are significantly different (p-value <0.05)). This result confirms the hypothesis that knocking out RBM20, which leads to larger isoform expression in titin, leads to a statistically significantly softer Young's modulus. While this result has been seen before in murine cardiac muscle, this is the first time this reduced stiffness has been confirmed in murine smooth muscle.

The direction of future study on this work is three fold. One, as seen from the histograms in Figure 2.5 there is a lot a variability within the cell averages, and the individual measurements for the knockout and wild-type cells. The AFM is known to be susceptible to machine noise, but the range of Young's modulus values obtained is attributed to more than machine noise. Further data collection could help to verify the presence of a binominal distribution, or reveal a more uniform average. Second, in Figure 2.5 F), there is some evidence of a cycle of fluctuations in Young's modulus for an individual cell. It would be worth further investigation into these fluctuations. Finally, work is being done by the collaborating scientists to quantitatively determine the difference in the level of expression of titin between the RBM20 knockout and the wild-type. However, titin expression in smooth muscle is low which means it is difficult to detect, and it's sequence is currently unknown. Determination of the difference in expression between the two cell types will strengthen any final conclusion made in the project.

Chapter 3

Measurement of Viscoelastic Materials

3.1 Introduction

So far Young's modulus has been determined by fitting force-indentation data with a Hertzian model. Recall that the Hertzian model assumes purely elastic behavior. Elastic response is essentially an objects tendency to deform under a load. In a purely elastic material there is no energy loss and no difference between the approach and retract curve. Herein lies the problem with using the Hertzian model to characterize cells. Many different cell lines have been tested and shown to demonstrate strong viscoelastic behavior in the cytoplasm and the nucleus [27].

Viscoelastic behavior is a combination of both a viscous and a elastic response to stress. A purely elastic material returns to its original state when the stress is removed as long as that the stress doesn't cause permanent alteration to the solid. Viscosity is a characteristic resistance to flow, and it manifests as a frictional energy loss. The more viscous a fluid the higher the frictional energy loss. Elasticity is typically a product of bond stretching along a crystal lattice in a ordered solid, where viscosity is the product of diffusion within a amorphous material. [29]. An example of a force curve for a purely elastic and for a viscoelastic sample are included in Figure 3.1.

The goal of this section is to measure the viscoelastic properties of different materials through the fitting of complex contact models to force-indentation curves. In order to use the contact models, there are a couple viscoelastic phenomena that are necessary to understand, primarily force relaxation and creep. When indenting on a viscoelastic sample if the indentation depth is kept constant the force on the sample will decrease (or relax) with time. If instead of controlling for the indentation depth the indentation force is kept constant then the sample will deform with time. Both of these concepts can been seen in the Figure 3.2. Understanding these viscoelastic phenomena is important to extracting viscoelastic parameters from force-indentation interactions.

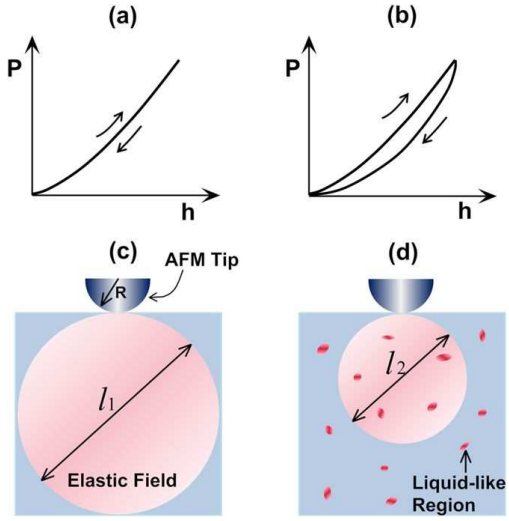

Figure 3.1: Comparison of a indentation retraction cycle for a purely elastic material (a) vs a viscoelastic material (b) show a schematic of a indentation for a elastic material (c) and for a viscoelastic material (d) [28]

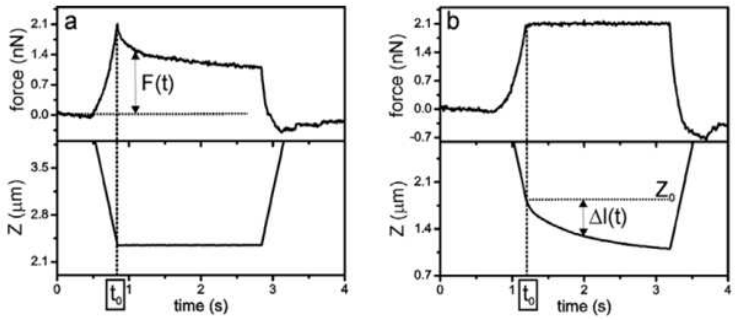

Figure 3.2: Force relaxation (a). In viscoelastic materials, constant indentation depth (Z(μm)) as a function of time leads to a decrease in the force (F(t)) on the sample. Creep(b). In viscoelastic materials constant indentation force (nN) as a function of time leads to a increase in the indentation depth (Δl(t)) on the sample. [30]

3.2 Specialized Probes for Cell Measurement

Typical AFM probe tips are on the order of 5-20 nanometers. This relatively sharp tip is necessary to give the AFM its nanoscale resolution, but when measuring on soft materials there are a few problems that arise. First, the microelectromechanical system (MEMS) used to generate probes from silicon is difficult to accurately control, leading to a ill-defined contact area that is difficult to accurately determine [31]. Second, during force-indentation measurements the typical force imparted on the cell is 2 nN. When the tip is 5-20nm, that is a lot of stress to place on a small area and it could be sharp enough to rupture the sample. The standard way to overcome both of these problems is to attach a polystyrene sphere with more determinable geometry and a radius of 1-50 μm . This large probe gives a more well defined contact area for model fitting, while also ensuring that our sample is deformed in a manner that results in minimal damage.

3.2.1 Collidial Probe Creation

The difficulty in creating colloidal probes arises from the scale of the fabrication. To give an idea of the scale a schematic of the cantilevers used in the fabrication process are given in Figure 3.3. The cantilevers used have the same schematics, however they do not have a tip on the edge.

The cantilever is large enough to see the geometry of the cantilever with the bare eye, but attaching a 10 μm polystyrene bead with accurate positioning is a challenge. To overcome the challenge of fine positioning a MP-285 micromanipulator from Sutter Instrument Company was used along with a bright field microscope capable of 40x magnification.

The fabrication process involves depositing a small volume of epoxy on the cantilever tip. This is done by using a copper wire that has been thinned by dissolving it in nitric acid. The copper wire is attached to a 3D printed probe holder which is then attached to the micromanipulator. Epoxy is spread onto a glass slide in a thin layer, the copper wire is then dipped into the glue. In order to optimize the amount of epoxy left on the wire, the wire is withdrawn from the glue and is indented onto a clean region until the drop of glue left behind is approximately the diameter of the beads

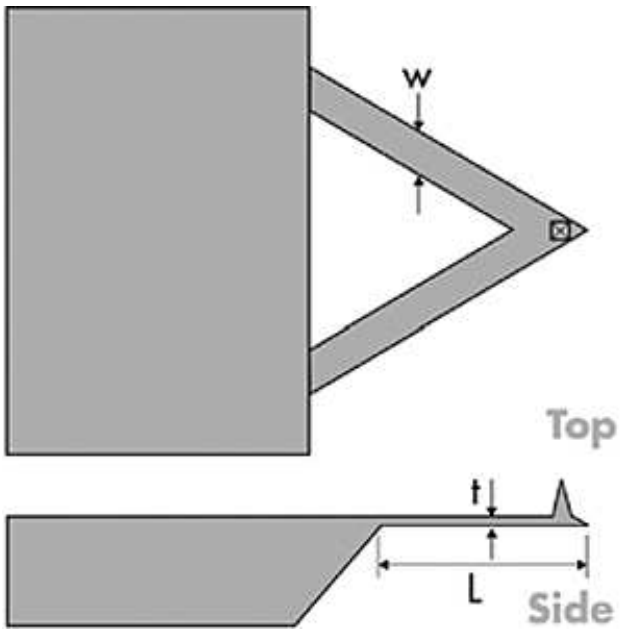

Figure 3.3: Diagram of the AFM Cantilevers used for collodial probe attachment. Where W= 20-30 μm, L= 200-210 μm, T= 0.55-0.65 μm [32]

that will be attached. The copper wire is withdrawn in the Z plane and the glass slide with epoxy is replaced with a dish with a soft gel bottom and a tip-less AFM cantilever. The AFM cantilever is brought in for focus of the microscope, the copper wire is brought as close to the tip as possible without touching until both the cantilever and the copper wire are visible in the microscope. The wire is then indented onto the cantilever towards the edge where the bead will be added. The copper wire is withdrawn and it is replaced with a new clean wire. The dish with the cantilever is also removed and replaced with a glass slide with polystyrene beads on its surface. A new thinned copper wire is used to place a 10 μm polystyrene bead on the small drop of epoxy.

An image of the micromanipulator on its 3D printed gantry is included Figure 3.4. The combination of the micromanipulator with the bright-field camera allows for fine positioning in real time.

3.2.2 Validation

It is possible to visually inspect these tips with a bright field microscope and insure that there is accurate X-Y positioning of the polystyrene bead on the AFM cantilever. However, when the beads

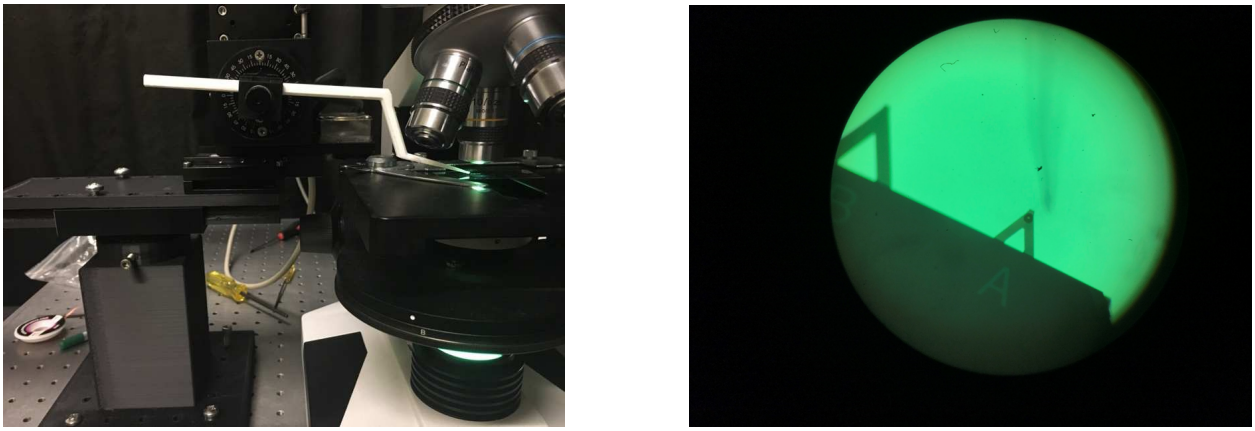

(a) **(b)**

Figure 3.4: Collodial Probe Setup and Optical view. View of the Micromanipulator attached to the 3D printed gantry . (a) 3D Gantry created by collaborator Adam McBride. (b) View through the optics when creating colldial probes . Note the thinned wire and the bead on the cantilever.

are viewed through the bright-field microscope there is limited Z information and it can become difficult to differentiate between a 10 μm bead and a 10 μm drop of glue. In order to ensure that the geometry of our tips is accurate Scanning Electron Microscopy (SEM) was used. The created probes were imaged with the assistance of Pat McCurdy. SEM images of the 10 μm bead and the 2 μm bead are included in Figure 3.5.

SEM confirmed that they geometry of the beads was ideal. Specifically the tips generated feature a small layer of epoxy which attaches the bead to the cantilever probe without entirely engulfing the bead. The next step is to ensure that the cantilevers can be operated with our existing AFM set up. To explore if our tips are functioning properly a TGX1 Test grating from Spectrum instruments was used as a calibration standard. One of the phenomena behind AFM is that the tip-radius in inversely related to image resolution. This makes sense because the AFM probe physically interacts with the sample. Smaller tips are capable of resolving smaller features at the trade-off of inducing more local stress. This validation step will utilize the inverse relationship between radius and resolution. The chosen grating has squares that are 1.2 μm wide, 0.6 μm tall and repeats with a spacing of 3.0 μm between each square. This means that the gap in between squares is slightly wider than the squares themselves (1.8 μm).

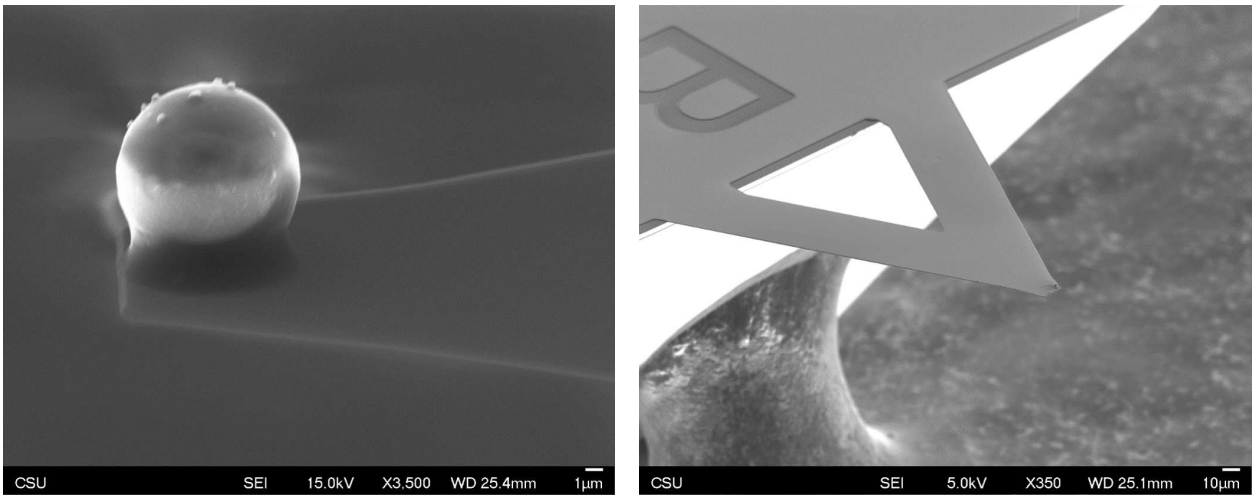

(a) **(b)**

Figure 3.5: 10 μm (a) and 2 μm (b) polystyrene bead attached to a NP-010 cantilever at 3,500X and 350X magnification respectively.

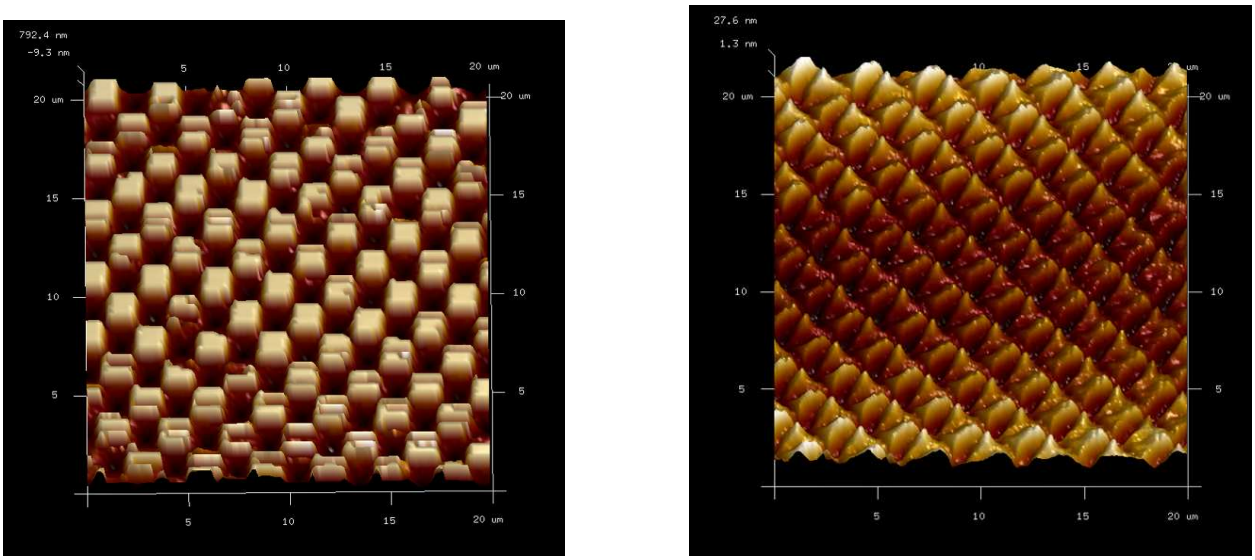

(a) TGX1 as scanned by a 2 μm polystyrene bead.

(b) TGX1 as scanned by a 10 μm polystyrene bead

Figure 3.6: TGX1 Test grating scanned by a 2 μm (a) and a 10 μm (b) polystyrene bead.

It is expected that the 2 μm bead should be able to resolve features significantly better than the 10 μm bead. The calibration standard was scanned by each tip in air in tapping mode. It was determined that there was a dramatic difference in feature resolution between the 2 μm bead and the 10 μm bead (see Figure 3.6).

3.3 Viscoelastic Model Analysis

Chapter 2 outlined the Hetrzian model which can be applied to force-indentation curves to pull out elastic modulus. As described in the introduction, the Hertzian model assumes that the sample is purely elastic. This assumption is quite wrong in the case of soft materials like cells. In order to accurately characterize the properties of a sample it becomes apparent that a more complicated contact model is going to be required. Recall a standard force-indentation curve from our studies Figure 3.7. The red line is the Hertzian model which allows for elastic modulus to be determined, but it is quite obvious there additional information present in this force indentation curve that is being ignored. In order to account for this behavior a model that allows for a time dependent relaxation modulus was used. The more complicated time dependent relaxation modulus is factored into the solution for a viscoelastic sample with a rigid spherical indenter. This model and the necessary Matlab code was graciously given to our lab by Armind Ravan's group from Purdue university.

3.3.1 Time-Dependent Relaxation Modulus

In order to account for the difference between the approach and retract curves it is necessary to introduce a time dependent relationship. Specifically for this case the time dependent relationship between shear stress σ(t) and shear strain ϵ(t). In this case σ(t) is a convolution of a time dependent relaxation modulus (E(t)) and the derivative of ϵ(t) with respect to time

$$\sigma(t) = \int_0^t E(t-\tau)\frac{d\epsilon(\tau)}{d\tau}d\tau \tag{3.1}$$

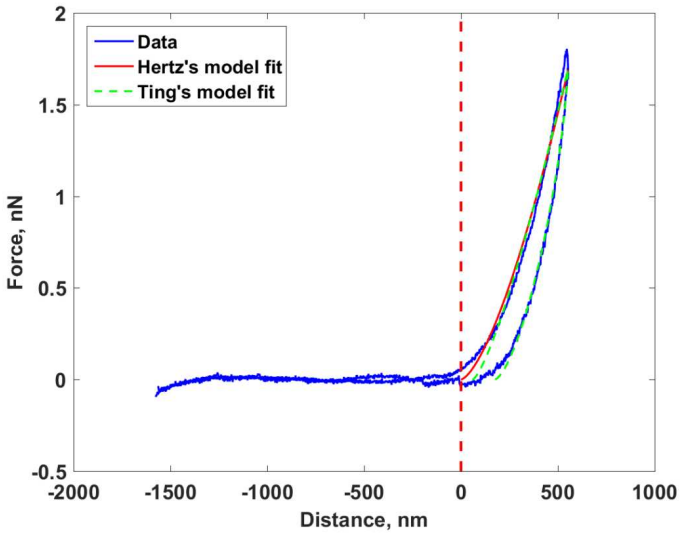

Figure 3.7: Example Force (nN) indentation (nm) curve taken on a HeLa Cell. The blue curve is the raw AFM data. The green dashed curve represents the fit of the Ting's Solution for a viscoelastic sample with a rigid spherical indenter.

Equation 3.1 can be slightly modified to apply to force indentation experiments where E(t) can be adjusted to different viscoelastic models. In this equation shear stress is related to force (F(t)), sheer strain is related to indentation (h(t)) and C captures the geometry of the indenter.

$$\mathbf{F}(t) = \frac{1}{C} - \int_0^t E(t-\tau)\frac{dh^n(\tau)}{d\tau}d\tau \tag{3.2}$$

Using the above equations Ramand's group was able to derive this equation which allows for force curve's approach and retract to be fit piecewise, accounting for any difference between the two. The solution has a couple distinct parts, first, a piece wise expression for force which depends on time and indentation as a function of time, an auxiliary function for determining $t_1(t)$, and two viscoelastic models.

$$\mathbf{F}(t,\delta(t)) = \begin{cases} \frac{4\sqrt{R}}{3(1-\nu^2)}\int_0^t E(t-\zeta)\frac{\partial\delta^{\frac{3}{2}}}{\partial\zeta}d\zeta & 0 \le t \le t_m \\ \frac{4\sqrt{R}}{3(1-\nu^2)}\int_0^{t_1(t)} E(t-\zeta)\frac{\partial\delta^{\frac{3}{2}}}{\partial\zeta}d\zeta & t_m \le t \le t_{ind} \end{cases} \tag{3.3}$$

$$\int_{t_1(t)}^t E(t-\zeta)\frac{\partial\delta^{\frac{3}{2}}}{\partial\zeta}d\zeta = 0, \tag{3.4}$$

$$\text{Standard Linear Solid (SLS)} \qquad E(t) = E_\infty + (E_0 - E_\infty)e^{\frac{-t}{\tau}} \tag{3.5}$$

$$\text{Power Law Rheology (PLR)} \qquad E(t) = E_0(1 + \frac{t}{t'})^{-\alpha} \tag{3.6}$$

[33]

Where F is the force on the cantilever tip. δ is the indentation depth. t is the time initiated at the time of initial contact ($t_m$is the duration of the approach phase and t_{ind} is the duration of the complete indentation cycle). t1 is the auxiliary function determined by Figure 3.4. ζ is the dummy time variable required for integration. E(t) is the time dependent Young's relaxation modulus. ν is the Poisson ratio which is assumed to be time independent. R is the radius of the indenter [33].

The SLS model is characterized by three parameters E_0, E_{inf} and τ. These are the instantaneous elastic modulus, the long term elastic modulus and the relaxation time respectively. The PLR model is characterized by two parameters, the instantaneous elastic modulus, E_0 , and the power law exponent α. Larger values of α result in larger relaxation. Materials with α=1 exhibit fluid like behavior, where materials with α=0 exhibit solid behavior. The equations above allow for experimental force curve data to be fit and extract viscoelastic parameters for a sample depending on the viscoelastic model chosen.

The SLS model captures both stress relaxation and creep behavior by combining a spring in parallel with a Maxwell element [34]. The Maxwell model consists of a linear spring element and a linear viscous dashpot element connected in series [35]. A modifed power law model can be obtained by replacing the dashpot element with a single spring-pot element [34].

3.4 Experiments

The goal of the final set of experiments was to test the colloidal probes along with the given algorithm for extracting viscoelastic parameters. First measurements were conducted on Poly Acrylamide (PAAm) hydrogels, and then on HeLa cells. PAAm hydrogels were made according to

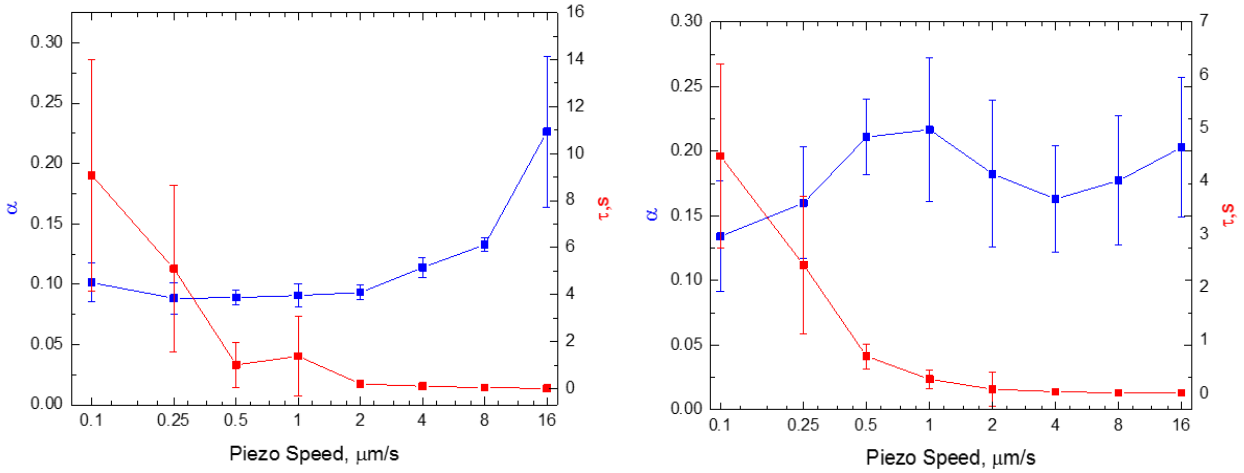

(a) PAAm. **(b)** HeLa Cell

Figure 3.8: Results of fitting the solution for a viscoelastic sample with a rigid spherical indenter. (a) PAAm. (b) HeLa Cells

.

a procedure by Saahil Sheth from Saint Loius University [36] with the help of Iain Bouringous in Dr. Bark's lab. Hela cells were cultured according to protocol (Appendix D) The fitting algorithm for extracting viscoelastic parameters was validated by Ramand the group by using both finite element analysis and AFM microrheology experiments. The goal was to see if it were possible to get the same trends in α and τ for PAAm hydrogels as a function of piezo displacement speed. Measurements on both PAAm hydrogels and HeLa cells were conducted at indentation speeds ranging from 100 nm per second to 16 μm per second. At each indentation speed, 100 force distance curves were collected. The force curves were put through the fitting algorithm provided by Ramand's group. In Ramand's groups results the hydrogels and live cells showed a increase in α with indentation speed, while τ decreased with indentation speed. It was the goal of these set of experiments to recreate the experiments as closely as possible, and determine if the model and the created collodial probes are viable for viscoelastic measurement.

3.5 Results

To determine α and τ the force-indentation curves at each speed were put through the Matlab algorithm developed by Yuri Efremov and the Ramand group. For each speed the algorithm was run twice, once for each model. As validation the hysteresis area was also calculated as a function of indentation speed. Our lab was able to obtain the same trend in α and τ in both PAAm hydrogels and in Hela cells. Specfically, α increases with increasing indentation speed and τ decreases with indentation speed. The results of the indentation experiment show that it would be possible for the Krapf lab to use the created colloidal probes in conjunction with the algorithm developed by Ramand's group to extract viscoelastic information from live cells and other viscoelastic samples.

Chapter 4

Conclusion

In this thesis the AFM was proposed as a investigative tool in three different experiments. First, AFM was used to investigate surface heterogeneity via inspection of the sample's topology. It was detremined that the PT/CS membranes had a high degree of heterogeneity and tensile strength on the order of human skin. Secondly, AFM force, indentation curves were combined with a Hertzian model to investigate the stiffness of murine aortic smooth muscle cells, and it was determined that a knockout of the RBM20 gene leads to significantly smoother cells. Finally, a technique for attaching collodial probes was presented, and validation that the model could be used to determine viscoelastic properties of samples was shown. Overall, it was shown that AFM is a powerful tool for inspecting the surface of a sample as well the material properties.

Bibliography

[1] Elias M Puchner and Hermann E Gaub. Force and function: probing proteins with afm-based force spectroscopy. *Current opinion in structural biology*, 19(5):605–614, 2009.

[2] JJ Saenz, N_ Garcia, P Grütter, E Meyer, H Heinzelmann, R Wiesendanger, L Rosenthaler, HR Hidber, and H-J Güntherodt. Observation of magnetic forces by the atomic force microscope. *Journal of applied physics*, 62(10):4293–4295, 1987.

[3] Cora-Ann Schoenenberger and Jan H Hoh. Slow cellular dynamics in mdck and r5 cells monitored by time-lapse atomic force microscopy. *Biophysical journal*, 67(2):929–936, 1994.

[4] K. Xu T. Kue D. Bailey T. Millar, A. Saikouski. Atomic force microscopy AFM. Technical report, University of Toronto, Advanced Physics Laboratory, 27 King's College Cir, Toronto, ON M5S, Canada, January 2016.

[5] M. Ganau. Nanotechnology applications in quantitative neuroscience: Proteomic analysis of malignant gliomas. 2013.

[6] Sudipta Seal. *Functional Nanostructures: Processing, Characterization, and Applications*. 01 2008.

[7] Srinivasa M Salapaka and Murti V Salapaka. Scanning probe microscopy. *IEEE Control Systems Magazine*, 28(2):65–83, 2008.

[8] Manfred Radmacher. Chapter 4 - measuring the elastic properties of living cells by the atomic force microscope. In Bhanu P. Jena and J.K. Heinrich HÃűrber, editors, *Atomic Force Microscopy in Cell Biology*, volume 68 of *Methods in Cell Biology*, pages 67 – 90. Academic Press, 2002.

[9] TCT Ting. The contact stresses between a rigid indenter and a viscoelastic half-space. 1966.

[10] Yueming Hua. Peakforce-qnm advanced applications training 2014. *Bruker. USA*, 2014.

[11] Subra Suresh. Biomechanics and biophysics of cancer cells. *Acta Materialia*, 55(12):3989–4014, 2007.

[12] Eleonore von Castelmur, Marco Marino, Dmitri I. Svergun, Laurent Kreplak, Zöhre Ucurum-Fotiadis, Petr V. Konarev, Alexandre Urzhumtsev, Dietmar Labeit, Siegfried Labeit, and Olga Mayans. A regular pattern of ig super-motifs defines segmental flexibility as the elastic mechanism of the titin chain. *Proceedings of the National Academy of Sciences*, 105(4):1186–1191, 2008.

[13] Shuichiro Higo, Yoshihiro Asano, Hisakazu Kato, Satoru Yamazaki, Atsushi Nakano, Osamu Tsukamoto, Osamu Seguchi, Mitsutoshi Asai, Masanori Asakura, Hiroshi Asanuma, et al. Isoform-specific intermolecular disulfide bond formation of heterochromatin protein 1 (hp1). *Journal of Biological Chemistry*, 285(41):31337–31347, 2010.

[14] Martin M LeWinter and Henk L Granzier. Cardiac titin and heart disease. *Journal of cardiovascular pharmacology*, 63(3):207, 2014.

[15] Wei Guo, Sebastian Schafer, Marion L Greaser, Michael H Radke, Martin Liss, Thirupugal Govindarajan, Henrike Maatz, Herbert Schulz, Shijun Li, Amanda M Parrish, et al. Rbm20, a gene for hereditary cardiomyopathy, regulates titin splicing. *Nature medicine*, 18(5):766, 2012.

[16] I Makarenko, CA Opitz, MC Leake, C Neagoe, M Kulke, JK Gwathmey, F Del Monte, RJ Hajjar, and WA Linke. Passive stiffness changes caused by upregulation of compliant titin isoforms in human dilated cardiomyopathy hearts. *Circulation research*, 95(7):708–716, 2004.

[17] Harvey Thomas Banks, Shuhua Hu, and Zackary R Kenz. A brief review of elasticity and viscoelasticity for solids. *Advances in Applied Mathematics and Mechanics*, 3(1):1–51, 2011.

[18] YC Fung. Elasticity of soft tissues in simple elongation. *American Journal of Physiology-Legacy Content*, 213(6):1532–1544, 1967.

[19] Meital Levy-Mishali, Janet Zoldan, and Shulamit Levenberg. Effect of scaffold stiffness on myoblast differentiation. *Tissue Engineering Part A*, 15(4):935–944, 2009.

[20] Girish Kumar, Christopher K Tison, Kaushik Chatterjee, P Scott Pine, Jennifer H McDaniel, Marc L Salit, Marian F Young, and Carl G Simon Jr. The determination of stem cell fate by 3d scaffold structures through the control of cell shape. *Biomaterials*, 32(35):9188–9196, 2011.

[21] Aleksandra R Nesic, Maja J Kokunesoski, Svetlana M Ilic, Milan V Gordic, Sanja B Ostojic, Darko M Micic, and Sava J Velickovic. Biocomposite membranes of highly methylated pectin and mesoporous silica sba-15. *Composites Part B: Engineering*, 64:162–167, 2014.

[22] Vinicius Borges V Maciel, Cristiana MP Yoshida, and Telma Teixeira Franco. Chitosan/pectin polyelectrolyte complex as a ph indicator. *Carbohydrate polymers*, 132:537–545, 2015.

[23] Narayan Bhattarai, Jonathan Gunn, and Miqin Zhang. Chitosan-based hydrogels for controlled, localized drug delivery. *Advanced drug delivery reviews*, 62(1):83–99, 2010.

[24] Yangchao Luo and Qin Wang. Recent development of chitosan-based polyelectrolyte complexes with natural polysaccharides for drug delivery. *International journal of biological macromolecules*, 64:353–367, 2014.

[25] Jéssica G Martins, Samira EA Camargo, Terrance T Bishop, Ketul C Popat, Matt J Kipper, and Alessandro F Martins. Pectin-chitosan membrane scaffold imparts controlled stem cell adhesion and proliferation. *Carbohydrate polymers*, 197:47–56, 2018.

[26] Ruei-Yi Tsai, Pin-Wen Chen, Ting-Yun Kuo, Che-Min Lin, Da-Ming Wang, Tzu-Yang Hsien, and Hsyue-Jen Hsieh. Chitosan/pectin/gum arabic polyelectrolyte complex: Process-dependent appearance, microstructure analysis and its application. *Carbohydrate polymers*, 101:752–759, 2014.

[27] Gernot Guigas, Claudia Kalla, and Matthias Weiss. Probing the nanoscale viscoelasticity of intracellular fluids in living cells. *Biophysical journal*, 93(1):316–323, 2007.

[28] YM Lu, JF Zeng, S Wang, BA Sun, Q Wang, J Lu, S Gravier, JJ Bladin, WH Wang, MX Pan, et al. Structural signature of plasticity unveiled by nano-scale viscoelastic contact in a metallic glass. *Scientific reports*, 6:29357, 2016.

[29] Marc AndrÃl' Meyers and Krishan Kumar Chawla. *Mechanical Behavior of Materials*. Cambridge University Press, 2 edition, 2008.

[30] Susana Moreno-Flores, Rafael Benitez, María dM Vivanco, and José Luis Toca-Herrera. Stress relaxation and creep on living cells with the atomic force microscope: a means to calculate elastic moduli and viscosities of cell components. *Nanotechnology*, 21(44):445101, 2010.

[31] Johann Erath, Stephan Schmidt, and Andreas Fery. Characterization of adhesion phenomena and contact of surfaces by soft colloidal probe afm. *Soft Matter*, 6(7):1432–1437, 2010.

[32] Bruker Corp. Afm probe catalog, 2017.

[33] Yuri M Efremov, Wen-Horng Wang, Shana D Hardy, Robert L Geahlen, and Arvind Raman. Measuring nanoscale viscoelastic parameters of cells directly from afm force-displacement curves. *Scientific reports*, 7(1):1541, 2017.

[34] Yuri M Efremov, Takaharu Okajima, and Arvind Raman. Measuring viscoelasticity of soft biological samples using atomic force microscopy. *Soft matter*, 16(1):64–81, 2020.

[35] Rui Miranda Guedes. *Creep and fatigue in polymer matrix composites*. Woodhead Publishing, 2019.

[36] Saahil Sheth, Era Jain, Amin Karadaghy, Sana Syed, Hunter Stevenson, and Silviya P Zustiak. Uv dose governs uv-polymerized polyacrylamide hydrogel modulus. *International Journal of Polymer Science*, 2017, 2017.

Appendix A

Book Chapter

In addition to the completion of the experiments described in this thesis, considerable time and effort went into writing a book chapter with Dr. Krapf. The Chapter focused on the physics of the plasma membrane. I wrote two sections of the chapter, one on membrane proteins and surface cell receptors and another chapter on Membrane fusion. The book is awaiting publishing, but the book chapter I assisted on has been accepted. The chapter is titled "Physics of the cell membrane" by Ben Ovryn, Terrance T. Bishop and Diego Krapf in "Physics-based methods in biological systems" Edited by Krastan Blagoev and Herbie Levine.

Appendix B

AFM Calibration Protocols

B.1 Deflection Sensitivity- the ratio of known cantilever movement distance to the photodetector signal output [nm/V]

1. Initialize AFM software and hardware, select "Mechanical properties"-"Quantitative Nanomechanical Mapping"-"PeakForce QNM in Air".

2. Load the fused silica or sapphire sample included in the PFQNM calibration standards kit.

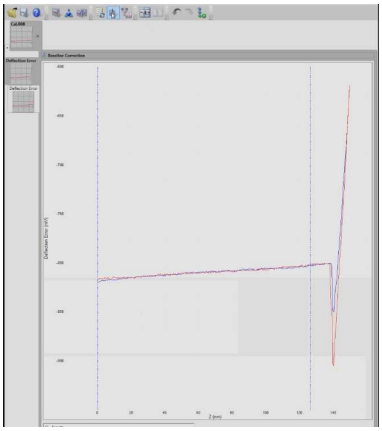

Figure B.1: Baseline correction on a calibration ramp. Note which button is baseline correction also note the position of the cursors on the non-contact region Adapted from Bruker PeakForce QNM Tip Calibration tutorial

3. Engage (make sure ScanAsyst Auto control is turned on).

4. If the center of the image is an area with height variations or obstructions offset the image to clean and flat region.

5. Switch to Ramp mode.

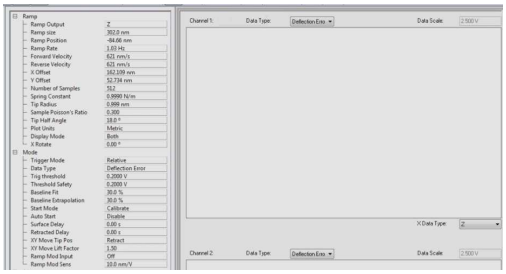

Figure B.2: Ramp parameters for a ScanAssist-Air probe on a Fused Silica sample adapted from Bruker PeakForce QNM Tip Calibration tutorial

6. Configure ramp parameters for the sample and the tip. Typical values are shown in Figure B.2

7. Make sure "channel 1" is set to plot "Deflection error vs Z".

8. Collect and save three force curves.

9. Open the three curves in Nanoscope Analysis.

10. For each curve do the following

    (a) Use the "Baseline correction" from the top menu to reset the deflection of the non-contact region to zero. Click execute to carry out the correction.

    (b) Fit cursors to the contact region of the curve by clicking on the left edge of the graph and dragging the cursor. (Control+click can be used to magnify a region of interest which can help when fitting contact region).

    (c) While the contact region is in the cursors go to menu bar, select commands and then select update sensitivity.

    (d) The software will return an updated sensitivity value in a dialogue box, record the value and accept the pop-up.

11. Calculate the average value of the obtained sensitivity - Select "Calibrate" from the menu bar- and enter the average value into the deflection sensitivity entry window.

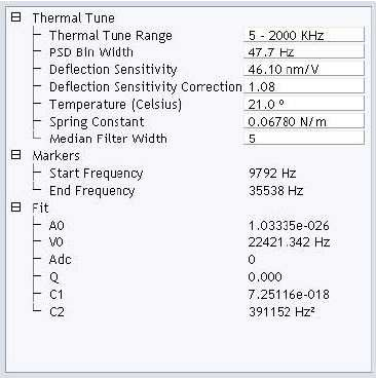

Figure B.3: Thermal Tune Parameters. Adjust Thermal Tune range so that the cantilever's resonant frequency is included. PSD Bin Width can be adjusted to reduce noise by averaging. Median Filter Width can be adjusted to remove narrow spikes

12. Deflection sensitivity is now calibrated, this calibration needs to be redone every time a probe is fixed to the probe head and the laser is aligned.

B.2 Thermal Tune - experimental determination of cantilever spring constant through thermal fluctuations

1. Click Withdraw a few times to achieve adequate separation between the sample and the tip.

2. Select Thermal Tune from the Toolbar - the thermal tune control window will launch.

3. Ensure that Thermal Tune parameters are appropriate for the tip. For example: the ScanAssist-Air probe has a resonant frequency of 70 kHz so it is important to use the 1-100 kHz tune range. See Figure B.3 for all Thermal Tune Parameters

4. Click acquire data and wait for the Power spectrum data to be plotted in the control window.

5. Place Cursor markers on opposite sides of the peak that correlates to the resonance frequency of the cantilever and select fit data

6. Select "Calculate Spring Constant" and select yes to automatically update the software with the calculated constant. This calibration is done only once for each given tip.

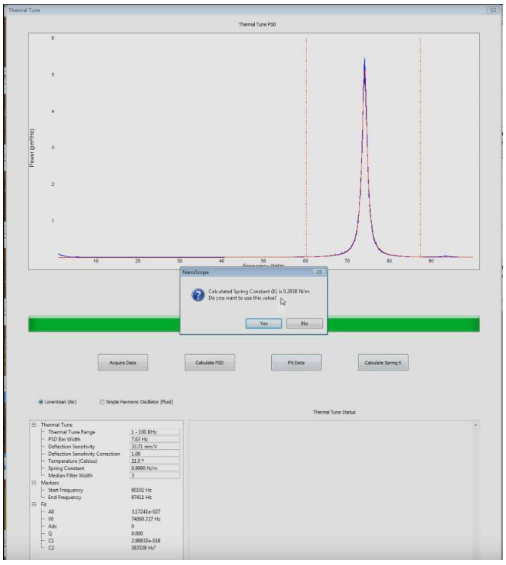

Figure B.4: Thermal Tune control window adapted from Bruker peakforce QNM tip calibration tutorial

B.3 Tip Radius - Experimental determination of the radius of the probe tip

1. Exchange the Silica sample for the Titanium Roughness sample.

2. Set up scan parameters. Scan size= 500nm- 1.5 μ X and Y offset=zero Scan Assist Noise Threshold =0.5 nm Aspect ratio= 1 or 2

3. Engage the Titanium sample

4. Collect a clean scan of the roughness sample and save this image

5. Open the roughness sample in the Nanoscope Analysis software

6. From the toolbar select âĂIJPlane FitâĂİ and conduct a first order plane fit on the obtained image.

7. From the toolbar select âĂIJQualify TipâĂİ. Select âĂIJEstimate TipâĂİ and the image will track its highest points. Be sure to keep this analysis file open and accessible during these next steps

8. Withdraw tip from the sample and exchange the titanium roughness sample for either of the two soft PDMS samples

9. Engage the sample and modify scan parameters to obtain good tracking of the surface.

10. Turn off ScanAssistAuto control and adjust peak force set point manually to obtain a noticeable deformation of the surface (5-10 nm).

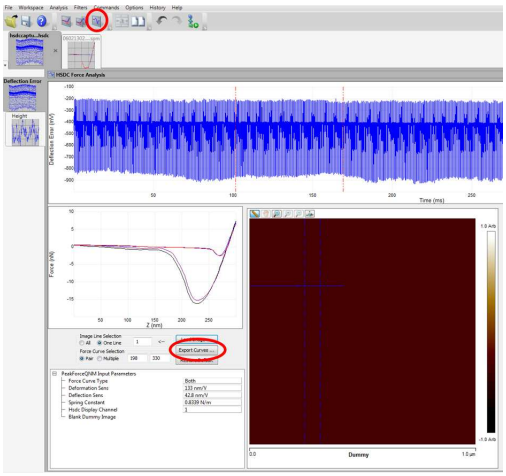

Figure B.5: High-speed Data analysis view within Nanoscope Analysis software

11. From the Peak force monitor window click the âĂIJCapture LineâĂİ command to open the high-speed data capture window

12. Acknowledge the data capture warning box.

13. In the high-speed data capture window click the Upload data button and note the fileâĂŹs appearance in the file cache.

14. Double-click the file icon to open it in Nanoscope Analysis.

15. Use the HSDC force curve analysis command to display individual force curves. Set cursors on typical data points and use âĂIJExport CurvesâĂİ command to save the selected force curves.

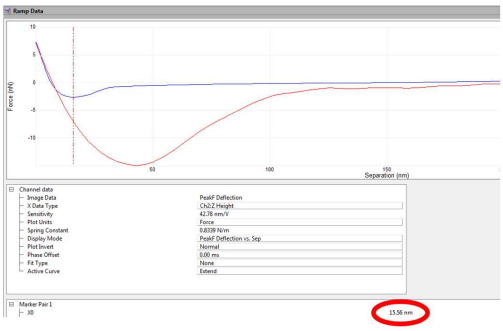

Figure B.6: Force vs Separation curve on a soft sample

16. Open the exported force curves and use the display parameters options to select peak deflection vs separation.

17. Place cursor on the point where the initial deflection begins and note the separation value

18. Select the previously captured Titanium roughness scan and enter the obtained separation value into the âĂIJHeight from Apex 1âĂİ field

19. Click qualify tip. The calculated radius will be displayed with the results.

20. The tip radius calibration is now done and in theory, only needs to be done once. Within the tip radius calibration, there is a tool that estimates tip quality which can be useful when determining the lifespan of a given tip.

21. Input calculated Tip radius into the cantilever parameters window.

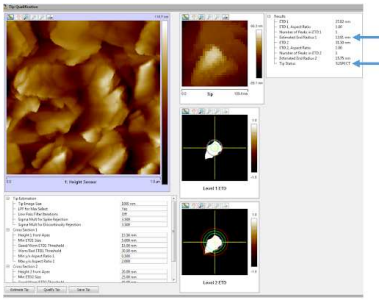

Figure B.7: Results from Tip Qualification. Note Tip Radius is stored as Estimated End Radius 1. The Tip Qualification also returns a Tip Status which can be used to determine the quality of the tip.

B.4 Additional Notes

1. If attempting to calibrate a tip for use in a fluid environment other than air, it is important to conduct the deflection sensitivity calibration and the thermal tune both in a fluid.

    (a) The deflection sensitivity calibration can be done in fluid on the bottom of a glass dish instead of the silica calibration standard.

    (b) The thermal tune is easily adjusted to fluid, just make sure the tip is submerged when data is collected

    (c) The tip radius calculation holds constant whether in fluid or in air so it is okay to do this tip calibration in either.

2. As mentioned in the specific sections each calibration has a window of viability.

    (a) The Deflection sensitivity calibration needs to be done each time the laser is aligned

    (b) The Thermal Tune needs be done only once for a tip

    (c) The Tip radius needs be done only once, but can be done again as measure of tip quality

3. The absolute method has two primary drawbacks

    (a) It is susceptible to accumulated errors

    (b) Time-consuming to perform

Appendix C

AFM Use Protocol

AFM use protocol.

1. Start Hardware before turning on software

   (a) For AFM turn on both switches under the pneumatic table, first the nano-controller (on top), then the power amplifier (on bottom)

   (b) Turn on the microscope by hitting the âĂIJ-âĂIJ button on the remote with the large ramâĂŹs head attached

   (c) Turn on the bruker vacuum module behind pneumatic table

2. Start Software

   (a) AFM-Left computer-Start Nano scope 9.3 and choose preferred experiment

      i. After choosing the preferred experiment an initialization dialogue will appear, before selecting yes check two things

      i. Gently tilt back the condenser

      ii. Ensure that the 10x objective is active and make sure it is in as low of a z position as possible.

   (b) NIS Elements (do not choose NIS Elements Analysis) -Right computer-select NIS Elements and select Andor driver if necessary

3. Prepare Probe holder and probe

   (a) Place preferred probe holder (either fluid or air) on silver bruker probe holder

   (b) Choose preferred probe for optimal imaging

   (c) Use tweezers to place selected probe on the probe holder, clamp the probe down. Ensure that the chosen tip is over the probe opening

(d) Place probe on AFM. It fits on easily one direction only. Do not force it.

4. Prepare Probe alignment

   (a) For fluid alignment prepare a dish of milli-q water.

      i. For optimal alignment and scanning performance ensure that levels of fluid used in alignment are equal to the levels of fluid in your sample.

   (b) Lower alignment stage-look on AFM software while you do.

      i. If alignment video feed is not showing go to tools–>video settings and change the video source

      ii. Use the knobs on the alignment stage to adjust the illumination and focus.

      iii. Turn illumination on to its highest levels and adjust focus until the tip is clear.

   (c) Adjust knobs on Resolve Head assembly that say âĂIJBeamâĂİ until the laser has been aligned to the exact spot of the tip on the cantilever

      i. Review brukerâĂŹs website if unsure of the tip position for a given cantilever

   (d) Adjust the âĂIJVâĂİ and âĂIJHâĂİ photo-detectors until watt output on bruker software has been maximized (I.E. adjust them until the red dot on the photo-detector is directly in the center of the cross hairs.

IF DOING MIRO PAUSE HERE AND MOVE TO AFM/CONFOCAL ALIGNMENT

5. Place sample on AFM stage and turn on vacuum

   (a) The control for vacuum is under Scan rather than Setup.

6. Move AFM head assembly over to AFM stage and lower gently, inserting the three assembly pegs into the AFM stage.

7. Adjust Scanning parameters to ideal settings

   (a) See brukerâĂŹs website for a description of each parameter

8. Use top view camera to find region of interest

    (a) Switch video feed from alignment stage over to the top view camera. (Tools-Video Settings)

9. Remove top view camera and close the pneumatic stage doors to minimize vibrations and increase image quality

10. Hit engage to begin scanning

    (a) You may want to lower the tip with the Z controller but be sure not to get too close to the sample

11. Offset can be used to adjust ROI without needing the top view camera

12. Save all scans in a consistent place.

13. Follow steps 1-3 backwards to reset the AFM for the next user.

Appendix D

Hela Cell Preparation protocol

This protocol describes preparing culture media and cell line maintenance. All work should be preformed in a biosafety cabinet.

D.1 Preparing Cell Media

1. Heat shock 50 ml aliquot of FBS. Let the FBS sit in water bath at 37°C for 1 hour after being thawed.

2. Thaw antibiotic. Do not let thawed antibiotic remain unfrozen for an extended amount of time.

3. Once FBS is thawed and heat shocked, add to DMEM

4. Pass DMEM+FBS+antibiotic solution through a bottle top filter into a sterile glass bottle.

5. Filter DMEM first, then add antibiotic. Add FBS at the end.

6. Label bottle with description, intials and date

7. Store media in fridge

Table D.1: Materials for HeLa cell culture media.

Material	Volume (ml)	Vendor	Product No.
FBS	50	Atlas Biologicals	EF-0500-A
DMEM (with phenol red)	500	Thermo Fisher Scientific	SH3002201
Sterile glass bottle	500	-	-
Bottle top filter	-	Life Science	CT-229717

Table D.2: Materials for splitting HeLa cells.

Material	Vendor	Product No.
Cell culture media	-	-
Trypsin	Thermo Fisher Scientific	25200114
Serological pipettes	-	-
35mm Delta T culture dish	Bioptechs	0420417B
100mm tissue culture dish	Life Science	CT-229620

D.2 Splitting Cells

Take extreme care to be as clean as sterile as possible. Always make sure to warm all solutions in water bath at 37°C before beginning the procedure.

1. A dish with confluent cells should be ready to split before beginning this protocol.
2. Label new dishes with initials, date, cell type and amount of cells.
3. UV all the culture dishes that cells will be split into for 30 min in the biosafety cabinet
4. Add 10 ml cell culture media from protocol D.1 into each new 100 mm dish
    (a) if live cell imaging is needed also add 1ml of culture media into 35 mm Delta T dishes
5. Place all dishes in the incubator until ready
6. Aspirate media from dish with confulent cells
7. Pipette 4 ml of Trypsin into the dish, and put it back into the incubator for 3 minutes
8. Once cells have lifted from bottom of dish, gently tap the dish to help with cell lifting
9. Add another 6 ml culture media into the dish
10. Centrifuge at 200g speed for 2 min
11. Aspirate the supernatant and resuspend the cell pellet with 5 ml culture media
12. Pipette proper amount of cells into each new dish then put them back in the incubator.

Appendix E

Binomial distribution equation

Binomial distribution was fit using origin student 2020, to the counts of all measurements conducted on wild-type cells. The following table will summarize the equation and parameterizations

Model	Gauss	
Equation	$y0 + \frac{A}{w\sqrt{\pi}} exp(-2(\frac{x-xc}{w})^2)$	
y0	3.66±0.45	3.66±0.45
xc	2.15±0.06	8.29±0.10
w	2.40±0.13	6.18±.22
A	220.60±13.54	616.09±18.80
R-Square	0.93	